JOURNAL OF AIRCRAFT
Vol. 48, No. 1, January–February 2011

Longitudinal Aerodynamics of a Vertical Takeoff and Landing Micro Air Vehicle

Ryan Randall,* Christian-Alexander Hoffmann,† and Sergey Shkarayev‡
University of Arizona, Tucson, Arizona 85721

DOI: 10.2514/1.C031044

The research and development efforts outlined in this paper address the aerodynamic design of micro air vehicles that are capable of vertical takeoff and landing, as well as hovering. The effect of a propulsive slipstream on a wing's quasi-steady aerodynamics is investigated as an early step toward improving existing vertical takeoff and landing designs and control algorithms. Wind-tunnel testing was conducted on a propulsion system with contrarotating propellers, a wing, and the combined wing and propulsion system. Aerodynamic coefficient definitions are discussed with regard to vertical takeoff and landing micro air vehicles, and modified definitions are presented.

Nomenclature

A	=	propeller disc area
C_D	=	wing drag coefficient (proposed)
C_L	=	wing lift coefficient (proposed)
c, $\bar{c}$	=	airfoil chord and mean aerodynamic chord of wing
D	=	wing drag
k	=	empirical constant for coefficient adjustment
L	=	wing lift
N	=	normal force on propulsion system
q, q_f	=	nominal freestream dynamic pressure and freestream dynamic pressure
Re	=	nominal freestream Reynolds number based on mean aerodynamic chord of wing
S	=	planform area of wing
S_f, S_s	=	planform area of wing not immersed in slipstream and area immersed in slipstream
T, T_0	=	thrust and static thrust (force generated by propulsion system in its axial direction)
V	=	nominal freestream velocity
V_f, V_s	=	freestream velocity and slipstream velocity
w	=	velocity increment added to flow by propulsion system
w_p, w_{p0}	=	velocity induced at propeller disc by propulsion system and static-induced velocity at propeller disc
X	=	horizontal aerodynamic force measured by balance
x	=	axial distance behind propeller discs
Y	=	vertical aerodynamic force measured by balance
α	=	angle of attack
δ_e	=	symmetric elevon deflection, positive downward
δ_t	=	throttle setting, varies from 0–100%
μ	=	absolute viscosity of local air
ρ	=	local air density

Received 29 March 2010; revision received 30 June 2010; accepted for publication 9 July 2010.

*Graduate Research Assistant, Department of Aerospace and Mechanical Engineering, 1130 North Mountain Avenue; Ryan18rmr@yahoo.com.

†Visiting Graduate Student, Department of Aerospace and Mechanical Engineering, 1130 North Mountain Avenue; chris.hoffmann84@gmail.com.

‡Professor, Department of Aerospace and Mechanical Engineering, 1130 North Mountain Avenue; svs@email.arizona.edu. Senior Member AIAA.

I. Introduction

MICRO air vehicle (MAV) design is gaining interest and becoming a significant field of research and study. MAVs that can operate autonomously are desirable; their applications include reconnaissance, urban surveillance, and detection of explosives, narcotics, and chemical weapons. There are different design classes of MAVs, which include fixed-wing, rotary-wing, and flapping-wing vehicles. Fixed-wing MAVs offer many attractive advantages over rotary-wing MAVs, including enhanced range, endurance, efficiency, and payload capacity. Unfortunately, fixed-wing MAVs have drawbacks, including their inability to hover, takeoff vertically, or land vertically. As a result, it is very difficult for them to operate effectively in urban environments and indoors. An attractive solution lies in development of vertical takeoff and landing (VTOL) MAVs that are capable of hovering, and which use a fixed wing.

An experimental study of propeller-induced flow on an MAV with a tractor configuration yielded interesting findings [1]. The angle-of-attack (AOA) range spanned by the study was from 0–44 deg. The study showed significant increase in lift, drag, and stall AOA with propeller slipstream strength. There was a notable downside: overall wing efficiency (lift-to-drag ratio) decreased.

A research project on fixed-wing MAVs capable of both hovering and vertical takeoff and landing was started at the University of Arizona [2]. The previous study [2] contrasted a tractor versus pusher configuration for propulsion. An 18% loss of thrust was observed when a pusher configuration was changed to a tractor configuration (due to parasitic motor drag). It is suspected that a well-shaped motor mount could reduce that loss, representing an avenue for future study. Lift and drag data were presented for the test subject's wing up to an AOA of 25 deg. The study [2] determined the slipstream effect on zero-lift wing drag and compared it with propeller momentum theory predictions. The present study describes a continuation of the project and investigates the quasi-steady aerodynamics of transition from horizontal to vertical flight and vice versa.

Of particular interest is the effect of the slipstream on wing aerodynamics over the entire flight domain. Slipstream effects include stall delay, lift augmentation, drag increase, and reduced aerodynamic efficiency [1]. A wealth of data is available from full-scale VTOL aircraft studies, which have resulted in the production of planes like the Harrier and the F-35, as well as tail-sitter designs (like the Ryan X-13) before them. Theoretical aerodynamic models for large VTOL aircraft are well developed and have been summarized in the literature [3,4]. Such models were developed for high Reynolds number (Re) flows over wings with relatively high aspect ratios (AR) in their prestall AOA regions. The current application requires aerodynamic modeling for low-Re low-AR wings throughout the prestall, stall, and poststall regions.

Existing studies on single-propeller slipstreams may offer some insight into increased wing drag. A previous study [5] experimentally

showed that the laminar-to-turbulent transition point moves closer to the leading edge of a wing (NACA 27-212 airfoil) when the wing is subjected to a propulsive slipstream. A turbulent boundary layer implies an increase in skin-friction drag that, for attached flow, dominates. Additional studies noted interesting slipstream-wing boundary-layer interactions. One paper [6] found that a propeller-induced slipstream does not eliminate laminar separation bubbles, and another paper [7] identified a cyclic change of the velocity profile of a boundary layer, between laminar and turbulent, which occurred at the same frequency as propeller rotation. The studies [5–7] were performed at Reynolds numbers greatly exceeding those typical for MAVs.

There are two overriding advantages that make the tractor configuration compelling in spite of documented drag penalties: 1) the slipstream's usefulness for providing control of the aircraft during hover and at low speeds, and 2) significant increases in maximum wing lift primarily due to stall delay.

The design of a VTOL MAV is largely affected by the following basic issues of the propulsion system itself: propeller torque, p factor, swirling slipstream, and gyroscopic moment. The typically small wingspans and ARs of VTOL MAVs result in low roll damping and low roll inertia, making them very sensitive to unbalanced propulsive torque. A prior study [2] noted a 90% decrease in net propulsive torque when two contrarotating propellers were employed, as opposed to a single propeller. Single-propeller propulsion systems have significant swirling in their slipstreams, which induces rolling moment as the stream strikes the rudder. Contrarotation negates swirl and prevents swirl-induced rolling moment. Unbalanced moment could be corrected with control surface deflection, but a drag penalty would be incurred.

Findings from the previous study [2] contributed to a very successful design. The University of Arizona, in collaboration with the Institut Superieur de l'Aeronautique et de l'Espace (ISAE) in France, has developed one of the world's smallest mission-capable fixed-wing VTOL MAVs: the Mini-Vertigo (Fig. 1a). The Mini-Vertigo has a flat-plate Zimmerman wing and is propelled by two motors and propellers that are contrarotating in a tractor configuration. The ability to hover and transition has been demonstrated on a radio-controlled prototype (capable of autonomous hovering flight [8]). Mini-Vertigo 2 (MV2) is the latest version of the Vertigo series of VTOL MAVs (Fig. 1b). MV2 is also capable of autonomy, which requires a functional autopilot. Autopilot control algorithms were addressed in a previous paper [9]. The algorithms were based on data from the present study.

To better fixed-wing VTOL MAV designs, a better understanding of the configuration's aerodynamics is pursued. Ultimately, empirical models should be developed to improve autopilot performance. In the current paper, quasi-steady longitudinal aerodynamics of transition are investigated through wind-tunnel testing and over the entire operating AOA range of these craft. Aerodynamic coefficient definitions will be considered and discussed with regard to fixed-wing VTOL MAVs.

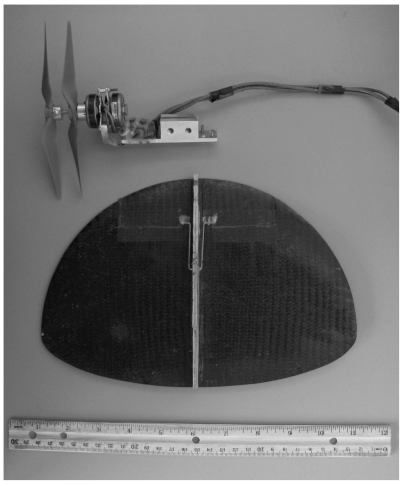

Fig. 2 Experimental model.

II. Test Subject

For continuity, the model used in this study is a replica of the model used in a previous study [2]. It was developed and tested at zero AOA at ISAE. The model consists of a Zimmerman wing and a coaxial propulsion system. To fit the experimental facilities at the University of Arizona, a different mounting system was developed. The experimental model for the present study is shown in Fig. 2; its specifications are shown in Table 1.

The propulsion system shown in Fig. 2 consists of two pairs of coaxial contrarotating motors and propellers with a cross shaft through both motors. This propulsion system was assembled using two brushless outrunners (MP Jet AC 22/4-60D) [10]. The motors are joined at their stator backplates and are regulated by an electronic speed controller (Phoenix-25), which provides the same rate of rotation to both motors.

The propellers used are from Advanced Precision Composites, with a diameter of 140 mm and a pitch of 114 mm. The distance between propellers is 13 mm, and the distance from the back of the aft propeller to the leading edge of the wing is 68 mm. The wing uses a very thin airfoil with a maximum camber of 3% located at $0.24c$; maximum inverse camber is 1% located at $0.85c$. Two elevons cover

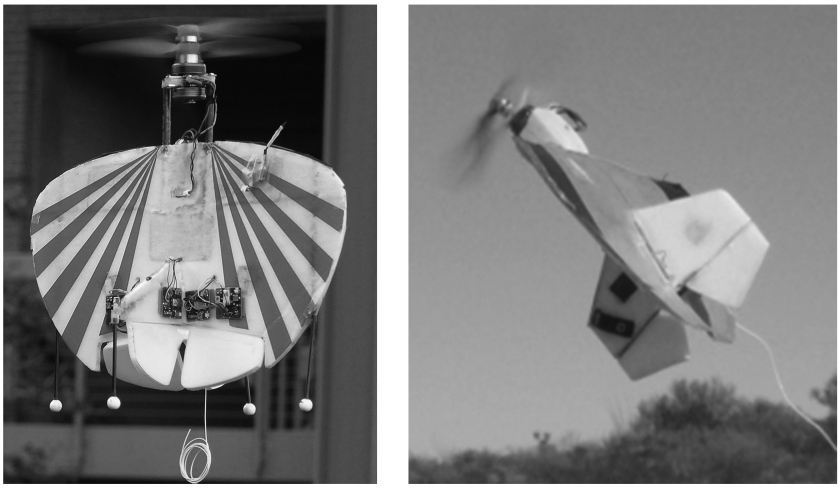

a) **b)**

Fig. 1 University of Arizona VTOL MAVs: a) mini-Vertigo in hover and b) MV2 in transition.

Table 1 Model information

Parameter	Value
Wingspan	252.0 mm
Mean aerodynamic chord	142.6 mm
Airfoil	S5010-TOP24C-REF
Planform shape	Zimmerman
Wing area	332.5 cm^2
AR	1.91
Total elevon area	41.0 cm^2
Root chord	168.0 mm
Contrarotating motors	MP Jet AC 22/4-60D
Propellers (2)	APC 5.5 × 4.5
Wing material	Carbon fiber
Rib material	Plywood
Motor mount material	Aluminum

12.3% of the wing's area. The wing is stiffened with a plywood rib along the root chord, as shown in Fig. 2.

III. Experimental Facility

The University of Arizona low-speed wind tunnel (Fig. 3) is an open circuit wind tunnel with a 0.9 × 1.2 m closed test section. The contraction ratio is 9.0, and the turbulence level is 0.3% for the range of speeds investigated.

The tunnel balance measures forces in all three spatial dimensions, but only force components in the longitudinal plane were analyzed in the present study. Balance calibration was performed daily by computing the calibration slope of each cell using calibrated weights. Strain gauges were debiased before each test run.

Fig. 3 Low-speed wind tunnel.

Pitch-control apparatus was developed for the model and can be seen in Fig. 4b along with other major components, which are labeled. The balance is located underneath the test section. The pylon connects to the balance, and so does a step motor to actuate the pitching apparatus. A power supply located outside of the test section powers the model's propulsion system. The pitching apparatus sweeps through a maximum of 50 deg, so the model was remounted to get higher angles in a separate test run. The installation in its 0–50 and 40–90 AOA configurations is shown in Figs. 4a and 4b, respectively.

Wind-tunnel tests were conducted at freestream velocities of 5, 10, and 15 m/s. The throttle setting was varied from 55 to 70% of full throttle. The case of zero motor power was also investigated, along with the effect of elevon deflection on lift and drag.

IV. Data Quality

AOA was determined using a digital inclinometer with a resolution of 0.1 deg. The AOA at each pitching-rod increment was determined by measuring the angle of the plywood rib while manually incrementing the pitching rod. The result was a degrees-per-click linear relationship. The procedure was executed twice. The relationship was found to be linear with a coefficient of variance of 0.9999. A zero-point drift test was conducted over the course of 25 tests. The initial AOA was checked and recorded. The maximum observed zero-point drift was 1.2 deg.

Because the bottom surface of the motor mount is rounded, uncertainty was present in aligning the thrust axis with the chord line. Misalignment was not expected to exceed 2 deg.

The accuracy of the force measurements was investigated by analyzing four data sweeps taken with no aerodynamic load, so lift and drag values were known to be zero. Sweeps spanned the range of the pitching mechanism used in actual testing. Balance data provided force measurements that were accurate to within 0.020 N for 560 collected points (lift and drag). Two sets of data go into determining the force on the wing, one subtracted from the other, suggesting a maximum error of 0.040 N. Higher force offset was observed in some of the data across the 0–50 and 40–90 sweeps.

The most significant source of force offset is probably solid-blocking related. The test section dynamic pressure was set to its desired value before turning on the propulsion system for each test run. Upon powering the propulsion system, there was an increase in dynamic pressure that was recorded at each AOA. As the model pitched upward, a steady drop in dynamic pressure was observed. The reset between test runs resulted in dynamic pressure profiles with discontinuities between 0–50 and 40–90 deg AOA sweeps, as shown in Fig. 5.

Some discrepancies in the data were observed around zero AOA. The testing apparatus was setup and resetup several times over the course of testing. The power wire (Figs. 4a and 4b) could not be reinstalled exactly the same way each time but was reinstalled approximately the same way based on photo documentation of prior setups. Any discrepancy in the setup would translate into error when

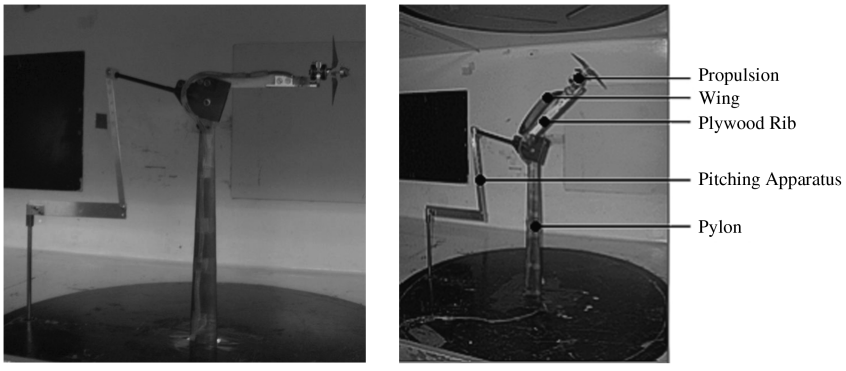

a) **b)**

Fig. 4 Setup of a) 0–50 AOA sweep and b) 40–90 AOA sweep.

subtracting out tare runs (taken during a different setup period). The resultant error is expected to be small, but for low AOAs, when measured forces are minute, the offset error could cause zero-AOA values at different throttle settings to appear inconsistent.

V. Propulsive Thrust

The propulsion system was evaluated on a motor testing bench in a previous study [2]. Variation of thrust, rotation rate, and propeller torque with throttle setting were obtained for both contrarotating tractor and pusher arrangements, as well as for a conventional single motor-propeller setup [2]. Induced-velocity estimates based on propeller momentum theory were in good agreement with experimentally measured values [2].

In the present study, the thrust axis is aligned with the wing's chord line and powered at 11.0 V, where thrust refers to the net aerodynamic force generated by the propulsion system normal to its propeller discs. Thrust and propeller rotation rate varied with three parameters: throttle setting, freestream velocity, and AOA. When the propulsion system was turned off and subjected to a freestream, drag on the system resulted in thrust values that were negative at low AOA. When subjected to 10 and 15 m/s freestream flows throttleoff thrust values were slightly negative, but as AOA increased, thrust values became slightly positive due to propeller windmilling.

Thrust can be used to estimate slipstream velocity based on classical propeller momentum theory. In the absence of a freestream, induced velocity at the propeller discs is determined by $w_{p0} = \sqrt{T/(2\rho A)}$. Propeller–ceiling interaction and ground effect contributed to an observed variation in static thrust with pitch angle.

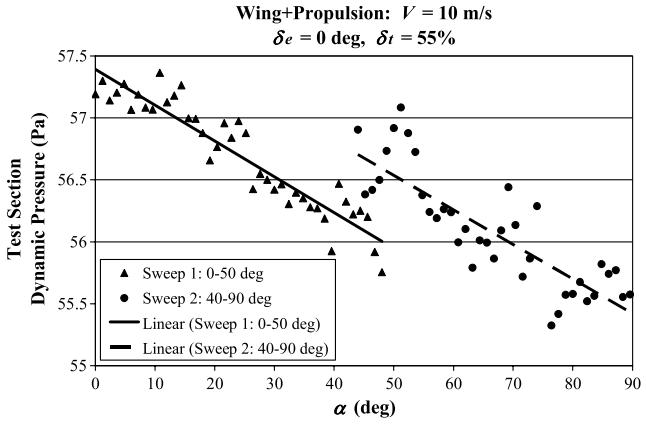

Fig. 5 Typical dynamic pressure variation with AOA.

Table 2 Throttle setting, static thrust, and static-induced velocity

δ_t, %	T_0, N	w_{p0}, m/s
55	1.14	5.8
60	1.61	6.9
65	2.01	7.7
70	2.47	8.5

The variation was relatively slight, never exceeding 4% of the mean thrust value for any throttle setting. Table 2 describes the relationship between throttle setting, static thrust, and static-induced velocity between the contrarotating propeller discs (velocity induced by both propellers combined). The first column of Table 2 refers to the percent of full throttle. Values in Table 2 are in good agreement with those obtained in a previous study [2].

Propulsion system AOA refers to the angle between the propeller disc axis and the freestream velocity vector. Figure 6 demonstrates that thrust increases linearly with throttle setting, and it decreases quadratically with freestream velocity at zero AOA, which was also observed in a previous study [2]. As freestream velocity toward the propeller disc (at zero AOA) increases, the difference between flow velocity into and out of the propeller disc decreases, along with thrust. This behavior is observed in several papers on propulsion, in which thrust coefficient is plotted against advance ratio [11,12]. One observation from Fig. 6 is that thrust-velocity variation depends strongly on AOA. Thrust decreases with freestream velocity at zero AOA, but it increases at 90 deg AOA.

Thrust curves in Figs. 7–9 are averaged between all sweeps, including the 40–50 deg AOA region where separate test runs overlap. Figure 7 shows that when the freestream velocity is 5 m/s, thrust increases linearly with AOA over the entire throttle setting and AOA domain. Note that thrust-curve slopes are independent of throttle setting. Thrust increases by as much as 22% between 0 and 90 deg AOA and by a factor of nearly 2.4 between 55 and 70% throttle.

As the freestream velocity increases to 10 m/s (Fig. 8), its effect on induced velocity over the face of the propeller disc increases. The slope of the thrust AOA curves has increased. The approximately linear relationship of thrust with throttle setting is generally maintained. The linear relationship of thrust with AOA begins to break down near the boundaries of the AOA domain, but it is preserved elsewhere. Similar to Fig. 7, the shape of each curve is approximately independent of throttle setting.

The relationship between thrust and AOA begins to take the form of a cubic polynomial as the freestream is strengthened to 15 m/s. Curve slopes near AOA boundaries approach zero, as seen in Fig. 9.

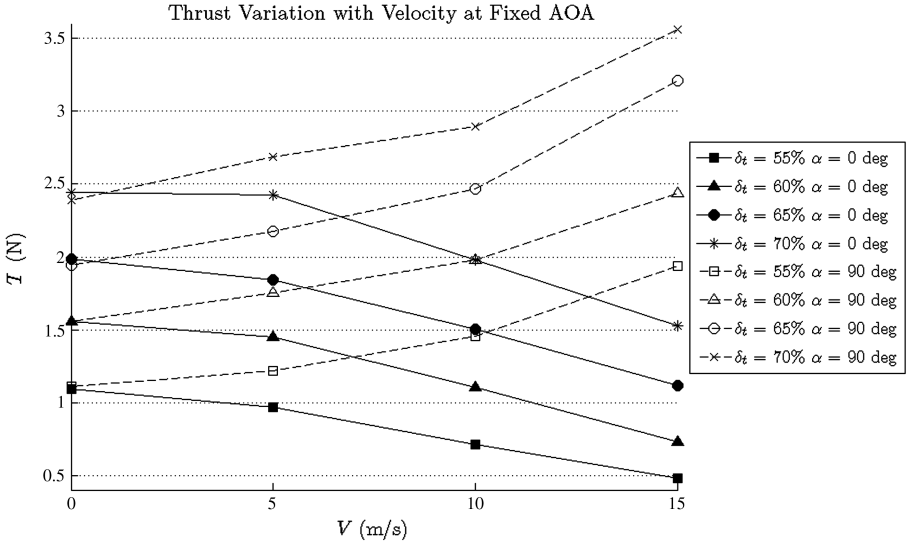

Fig. 6 Variation of thrust with freestream velocity at 0 and 90 deg AOA.

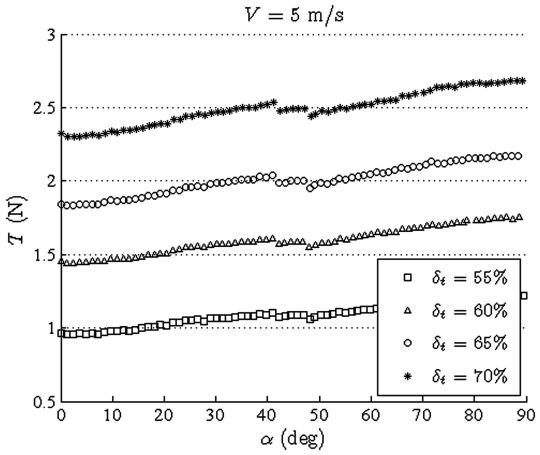

Fig. 7 Thrust variation in the presence of a weak freestream.

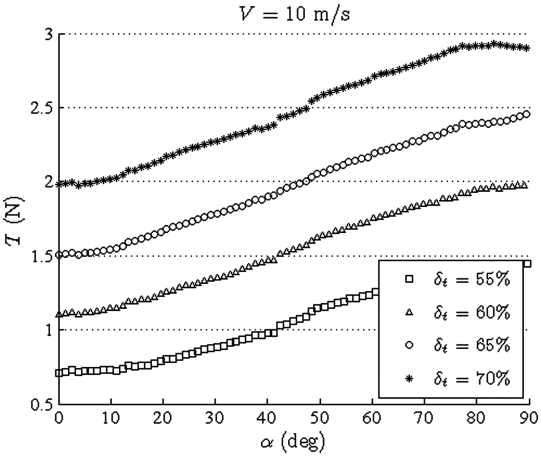

Fig. 8 Thrust variation in the presence of a moderate freestream.

Thrust-AOA curves are shifted in a roughly linear fashion as the throttle setting is varied, especially near 45 deg AOA. Notice that at zero AOA (in Figs. 7–9), the change in thrust with the throttle setting is approximately 0.4 N per 5% throttle, independent of freestream velocity.

VI. Wing Aerodynamic Forces

Wing aerodynamics were investigated using the assembly of the wing and contrarotating motors and propellers, as described in Sec. III. In this case, the aerodynamic balance measured a horizontal component X and a vertical component Y of the total force applied to the model. To determine the lift L and the drag D on the wing, propulsive thrust and normal force projections are subtracted from respective components of the total force as

$$D = X - T\cos\alpha + N\sin\alpha \tag{1}$$

$$L = Y - T\sin\alpha + N\cos\alpha \tag{2}$$

This procedure is illustrated in Fig. 10. Note that the thrust axis is aligned with the wing's chord line. Aerodynamic forces are produced by two mixing flows: the freestream and the propulsive slipstream.

A. Lift

In Figs. 11–13, the variation of wing lift with AOA is presented. Force data were averaged in the overlapped region (between the 0–50 and 40–90 deg AOA sweeps). The region may appear rough, because dimensional data do not account for discontinuity in dynamic pressure. Plots are distinguished by their nominal freestream velocities. The relationship between nominal freestream velocity, dynamic pressure, and Reynolds number is presented in Table 3. The Reynolds number is referenced to the mean aerodynamic chord of the model and nominal freestream velocity.

There are some common features in Figs. 11–13. The figures show that the propeller slipstream has a strong stall-delay effect and a stall-softening effect over the entire testing domain (loss of lift is less abrupt near stall), and that prestall lift-curve slope increases with increasing throttle setting.

In Fig. 11, stall AOA moves from 21 deg to about 45 deg. Maximum wing lift increases by 230%. There is a downward shifting of the curves, with increasing throttle setting at zero AOA. With only a weak freestream, at 90 deg AOA, the slipstream blows downward

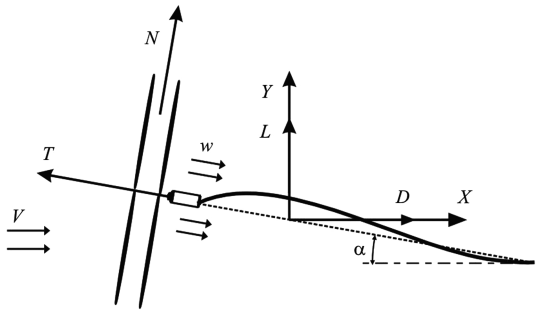

Fig. 10 Orientation of forces.

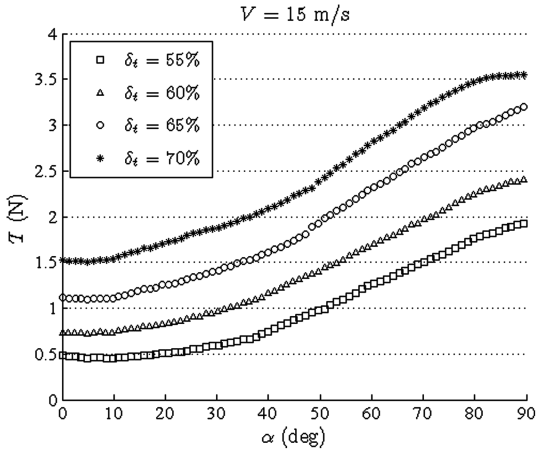

Fig. 9 Thrust variation in the presence of a strong freestream.

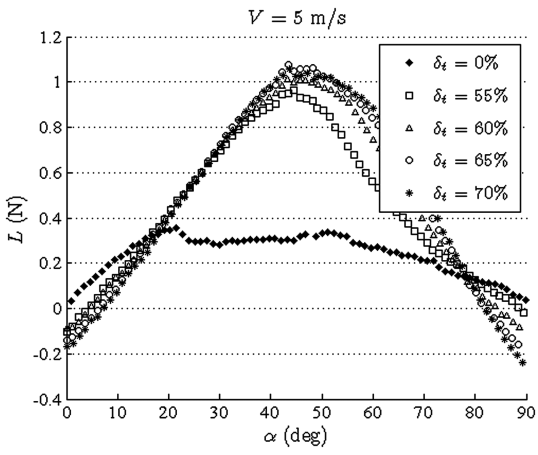

Fig. 11 Variation of wing lift for $\delta_e = 0$ deg and $V = 5$ m/s.

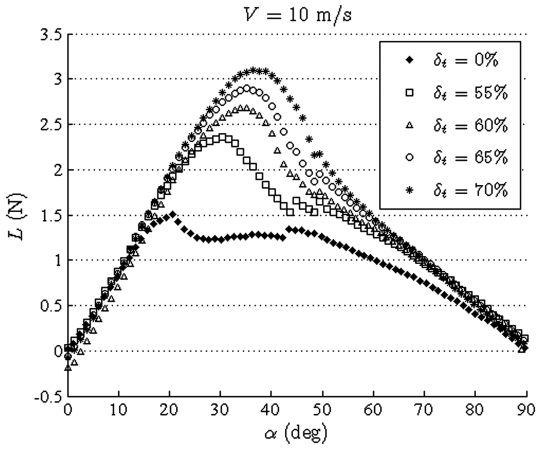

Fig. 12 Variation of wing lift for $\delta_e = 0$ deg and $V = 10$ m/s.

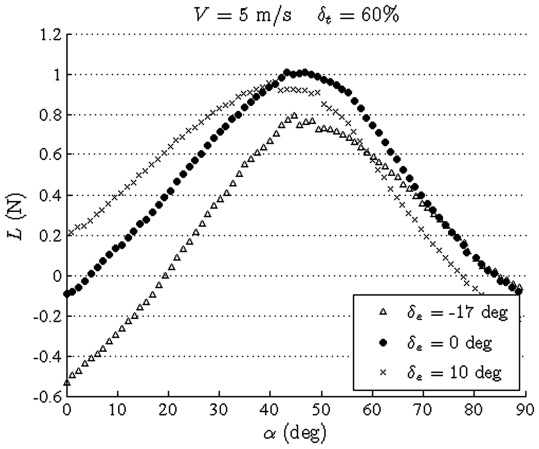

Fig. 14 Variation of wing lift for $\delta_t = 60\%$ and $V = 5$ m/s.

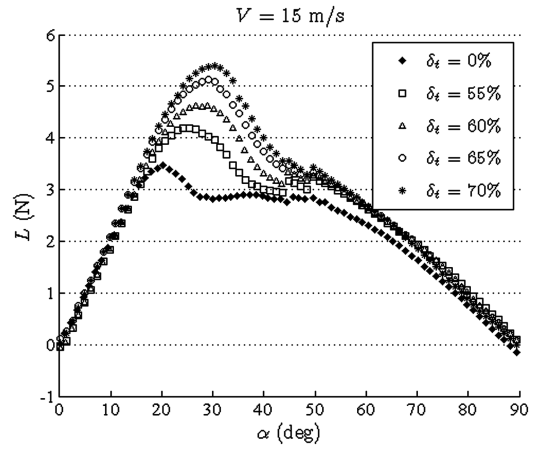

Fig. 13 Variation of wing lift for $\delta_e = 0$ deg and $V = 15$ m/s.

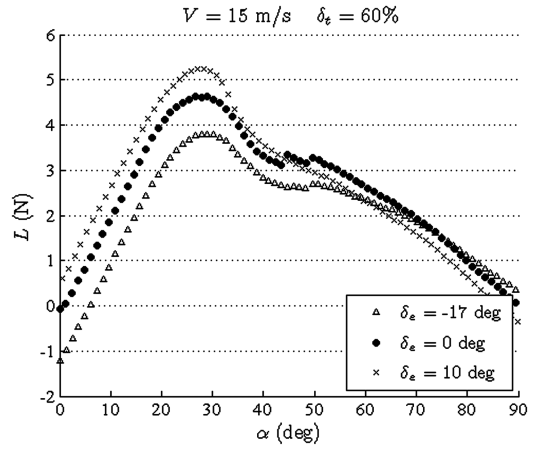

Fig. 15 Variation of wing lift with AOA and elevator deflection, $V = 15$ m/s.

over the wing (opposite the direction of lift), generating a friction-related downward force (negative lift).

In Fig. 12, the freestream is 10 m/s, which is stronger than in the previous plot. The relative effect of the slipstream is reduced. Notice that the wing produces approximately zero lift near 0 and 90 deg AOA under power-on conditions. Stall is delayed from 20 to 38 deg at 70% throttle. Maximum lift increases 100% due to both stall delay and lift-curve slope increase. The origin (zero AOA) of the 60% curve seems slightly inconsistent. Error near zero AOA was discussed in the Sec. IV.

Figure 13 corresponds to the strongest freestream setting, 15 m/s. Stall is delayed from 20 to 31 deg with a maximum increase in wing lift of 55%. Lift-curve slopes are slightly increased with throttle setting. All curves produce nearly zero lift at 0 and 90 deg AOA.

Next, the effect of elevator deflection on wing lift is considered. Tested elevator deflections were selected based on Mini-Vertigo flight-test data and mechanical restrictions. Figures 14 and 15 have averaged data in the sweep-overlapped region. The figures are dimensional; they are not adjusted for dynamic pressure variation. Both figures show an increase in lift at zero AOA with positive elevator deflection. Lift is always higher at higher elevator deflection in the linear lift-curve slope region. There is a decrease in lift with positive elevator deflection at 90 deg AOA. Stall AOA decreases as elevator deflection increases.

Figure 14 shows that elevator deflection at $V = 5$ m/s (low Reynolds number) has a significant impact on lift-curve slope. Slopes decrease for increasing elevator deflection. Maximum lift is highest at zero-elevator deflection.

The effect of elevator deflection on lift-curve slope is greatly diminished as freestream velocity is increased to 15 m/s, as seen in Fig. 15. Maximum lift increases with increasing elevator deflection. The effect of elevator deflection is to shift the lift curves in the prestall region. It has a minor effect on stall AOA. At 90 deg, lift decreases with increasing elevator deflection, similar to Fig. 14.

Table 3 Velocity, dynamic pressure, and Reynolds number

V, m/s	q, Pa	Re
5	13.7	43,000
10	55.3	87,000
15	124.4	130,000

B. Drag

Drag data are presented in Figs. 16–18. Drag data have considerably less offset between sweeps and were measured with one load cell only (as opposed to three cells used in lift measurements). The very small magnitude of measured forces has contributed to some irregularities in the data near zero AOA. Figures 16–18 demonstrate that drag is concave-up parabolic in the prestall region and concave-down parabolic in the poststall region, regardless of freestream velocity or throttle setting. Drag curves appear distorted in the stall region. Maximum drag increases with throttle setting, and wing aerodynamic efficiency is reduced by the slipstream.

In Fig. 16, drag increases continuously with AOA when the throttle is off, but when the slipstream is present (and sufficiently strong), drag reaches its maximum between stall and 90 deg. Maximum drag

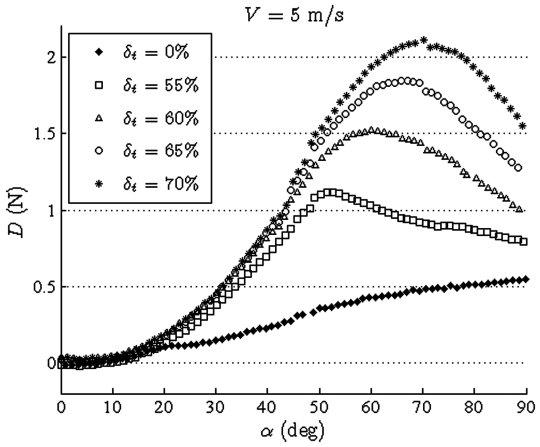

Fig. 16 Drag in the presence of a weak freestream.

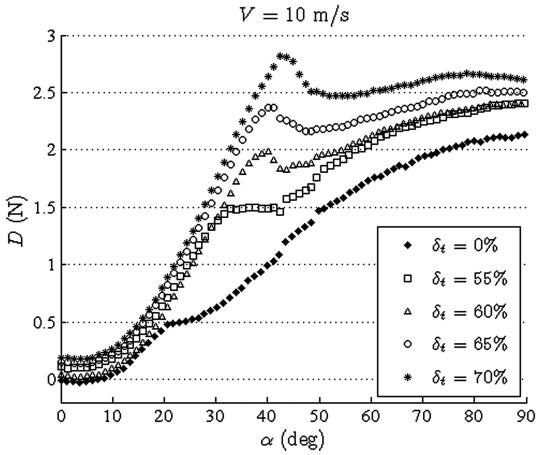

Fig. 17 Drag in the presence of a moderate freestream.

on the wing increases 285% between 0 and 70% throttle. Drag at low AOA is below expectation due to offset error.

In Fig. 17, the freestream is 10 m/s. Increased freestream strength causes throttle-on curves to move closer to throttleoff curves in the poststall region, and it causes maximum drag to move to 90 deg AOA for all but the 70% curve. The curves show general increase in wing drag with the throttle setting near zero AOA. Maximum drag increases by 32% as a result of the slipstream. One interesting aspect of Fig. 17 is the spikes that occur a few degrees after stall AOA. The spikes are unique to the 10 m/s freestream plot and throttle settings above 55%. In Fig. 16, the 55% throttle curve is approaching a spikelike condition, and so is the 70% curve in Fig. 18. Observations suggest that qualitative drag behavior is highly dependent on the relative strength of the freestream and slipstream.

Figure 18 shows increase in drag with the throttle setting in the stall and poststall regions. The freestream is strong: 15 m/s. Near-continuous increase in drag with AOA is present for all curves. Separation of the curves is most apparent between 20 and 40 deg AOA, where stall is taking place on the corresponding lift curve. Relative to Figs. 16 and 17, the slipstream has a considerably smaller effect on drag. Maximum drag is increased less than 5% by the slipstream. Inconsistency in curve origins suggests offset error in the 0–40 AOA region.

Figure 19 describes the variation of drag with elevator deflection. Minimum drag AOA increases with decreasing elevator deflection as it tracks zero-lift AOA. At 90 deg, drag is highest for zero-elevator deflection, which is when the projected frontal profile area of the wing is greatest. Figure 19 shows that maximum drag AOA increases with decreasing elevator deflection for weak freestreams ($V = 5$ m/s).

VII. Nondimensional Coefficients

The effect of the slipstream on dimensional wing aerodynamics was characterized in the previous section. Attention is now turned toward coefficients for zero-elevator deflection data. Aerodynamic coefficients are obtained from force data. Traditionally defined coefficient curves are shape similar to the dimensional curves presented, with some distortion owing to dynamic pressure variation with AOA.

Traditional definitions of lift and drag coefficients break down when they are applied over the entire operational domain of a VTOL MAV. Namely, coefficients approach infinity as forward speed goes to zero in the absence of wind (hover), in which case Reynolds number goes to zero.

A means of nondimensionalization that is finite and continuous from zero freestream velocity through 15 m/s is desirable. Because of the changing nature of the flow physics throughout the domain, development of an appropriate nondimensionalization procedure is not trivial. Stall AOA and maximum lift depend on the relative strength of the slipstream to the freestream, as do key features of drag curves. In-depth investigation of the relative strength effect is left to future studies.

Previously developed semiempirical VTOL models have used slipstream dynamic pressure to nondimensionalize coefficients [3,4]. The slipstream-based approach prevents coefficient divergence, but it does not capture the physical influence of the freestream-immersed region of the wing. This study proposes (to the authors' knowledge) a new formulation, which considers both regions.

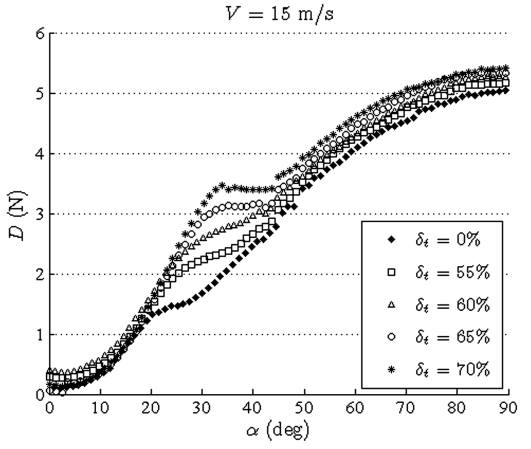

Fig. 18 Drag in the presence of a strong freestream.

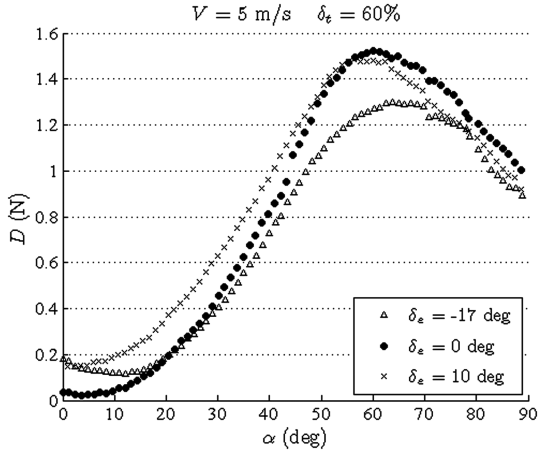

Fig. 19 Variation of wing lift with AOA and elevator deflection, $V = 5$ m/s.

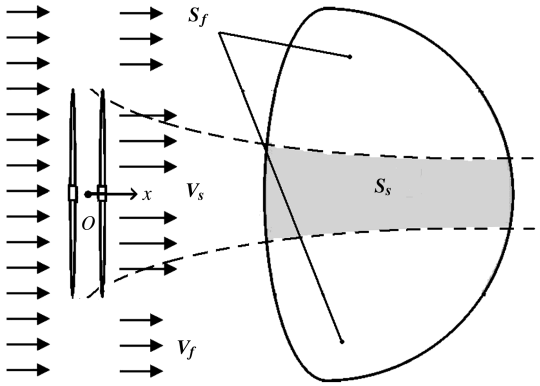

Fig. 20 Slipstream—freestream model.

A. Aerodynamic Model

The parameters specified in Fig. 20 are used in proposed coefficient definitions. A discussion of parameter determination follows. In Fig. 20, the diameter of the slipstream (assumed to be a stream tube) varies with axial distance behind the propeller discs, x. The axial variation of stream tube diameter is determined from continuity and given by [13]

$$d = d_p\sqrt{w_p/w} \tag{3}$$

where w_p is induced velocity between the propeller discs (the origin O in Fig. 20) and w is induced velocity some axial distance x behind the propeller discs (determination of w_p and w is discussed later). The diameter of a given propeller, d_p, is typically known. Slipstream-wing area S_s is determined via integration over the planform of the wing. Freestream wing area S_f is the difference between total wing area and slipstream-wing area. Freestream velocity V_f is generally known, while slipstream velocity V_s is not. Velocity w_p must be determined to estimate slipstream velocity and stream tube diameter. One approach to determining induced velocity at the propeller disc uses Glauert's hypothesis [13]:

$$T = 2\rho A V_p w_p \tag{4}$$

V_p is the flow speed at the propeller discs; it is given by [13]

$$V_p = \sqrt{(V_f\cos\alpha + w_p)^2 + (V_f\sin\alpha)^2} \tag{5}$$

Figure 21 depicts the parameters in Eq. (5); the rectangle represents propeller discs viewed from the side.

Combining Eqs. (4) and (5) and solving for w_p yields [13]

$$w_p^4 + 2w_p^3 V_f\cos\alpha + w_p^2 V_f^2 = \left(\frac{T}{2\rho A}\right)^2 \tag{6}$$

The quartic Eq. (6) may be solved for w_p numerically; all other quantities are known or have been experimentally determined.

The propeller-induced velocity a distance x behind the propeller discs is given by

$$w(x) = w_p\cdot\left[1 + \frac{2x/d_p}{\sqrt{1+(2x/d_p)^2}}\right] \tag{7}$$

As a check on the validity of Eqs. (6) and (7), $w(x)$ was calculated for a few special cases (zero AOA, zero V_f, and same T/ρ) and compared with hot-wire measurements from a previous study [2]. Induced-velocity calculations were in good agreement with radius-averaged measurements from the previous study [2].

A characteristic slipstream velocity as a function of distance behind the propeller discs and AOA can be defined as

$$V_s(x) = \sqrt{[V_f\cos\alpha + w(x)]^2 + (V_f\sin\alpha)^2} \tag{8}$$

Equation (8) shows that slipstream velocity is equal to freestream velocity when induced velocity is zero. $V_s(x)$ may be averaged based on slipstream-immersed wing area to obtain $\bar{V}_s$:

$$\bar{V}_s = \frac{\int V_s\,\mathrm{d}S_s}{S_s} \tag{9}$$

The parameters defined in Fig. 20, for which determination was just covered, are applied to new coefficient definitions. Lift and drag coefficients include a sum of slipstream and freestream dynamic pressures. The wing area over which the corresponding dynamic pressures act is the basis for their scaling. In the proposed model, lift and drag coefficients are finite and continuous over the entire domain, and the Reynolds number is always nonzero:

$$Re = \frac{\rho\cdot\bar{c}}{\mu\cdot S}\cdot(\bar{V}_s S_s + V_f S_f) \tag{10}$$

$$C_L = \frac{2L}{\rho\cdot(\bar{V}_s^2 S_s + V_f^2 S_f)} \tag{11}$$

$$C_D = \frac{2D}{\rho\cdot(\bar{V}_s^2 S_s + V_f^2 S_f)} \tag{12}$$

Results of applying the proposed model to data presented in Secs. III and VI are provided in Tables 4 and 5. Of primary interest is the prestall region where the lift-curve slope is expected to increase slightly with the Reynolds number. Notice that proposed slopes decrease with the proposed Reynolds number. A probable reason for the observation is the tendency of a slipstream to prematurely transition a boundary layer to turbulence [5,7], causing a disproportionate effect on viscous forces relative to inertial forces. An empirical adjustment (to avoid introduction of further nondimensional parameters) may be used to compensate for the effect, or the proposed Reynolds number may be redefined.

Table 4 Proposed coefficient lift-curve slope for AOA 0–10 deg

Thr/V, %	5 m/s	10 m/s	15 m/s
0	2.38	2.57	2.65
55	0.69	1.92	2.60
60	0.50	1.43	2.45
65	0.43	1.13	2.27
70	0.37	0.97	1.86

Table 5 Mean proposed Reynolds number (in thousands) over AOA 0–10 deg

Thr/V, %	5 m/s	10 m/s	15 m/s
0	44	87	130
55	85	104	136
60	96	119	140
65	103	131	148
70	113	142	160

Table 6 Percentage increase of w_p for AOA 0–90 deg

Thr/V, %	5 m/s	10 m/s	15 m/s
55	14	150	584
60	11	75	359
65	10	64	256
70	8	42	146

Table 7 Lift-curve slope for AOA 0–10 deg, with $k = 0.19$

Thr/V, %	5 m/s	10 m/s	15 m/s
0	2.39	2.59	2.65
55	2.68	2.62	2.75
60	2.45	2.73	2.76
65	2.45	2.68	2.78
70	2.45	2.69	2.81

Table 8 Mean proposed Reynolds number (in thousands) for AOA 0–10 deg, with $k = 0.19$

Thr/V, %	5 m/s	10 m/s	15 m/s
0	43.5	86.9	130
55	46.7	89.0	131
60	47.8	89.7	132
65	48.7	90.6	132
70	49.5	91.4	133

Another drawback of the proposed model is its complexity. A major hurdle to the application of Eqs. (10–12) is the difficulty associated with computation of w, which requires calculation of w_p (nonlinear). As the distance from the propeller discs, thrust, freestream velocity, and AOA changes, w changes. Other parameters depend on varying w.

B. Empirical Correction to Aerodynamic Model

Simplifying assumptions are introduced to reduce the complexity of aerodynamic coefficient calculations:

1) The slipstream is fully contracted over the wing (d, S_s = constant).

2) The slipstream velocity does not vary with distance behind propeller discs ($w = w_p$, $V_s = V_p$).

3) The variation of w_p magnitude with AOA is negligible.

4) The induced velocity w can be scaled by a constant empirical factor k to compensate for premature boundary-layer transition.

Applying assumptions 1–4 leads to

$$w = kw_p \tag{13}$$

$$w = \frac{k}{2}\left[\sqrt{V_f^2 + \frac{2T}{\rho A}} - V_f\right] \tag{14}$$

$$\bar{V}_s = \sqrt{(V_f \cos\alpha + w)^2 + (V_f \sin\alpha)^2} \tag{15}$$

In the present study, d over the wing varies from 106.5 mm at the leading edge to 100 mm at the trailing edge. Fully contracted d is 99 mm, justifying assumption 1. In the present case, w and V_s can increase, at most, 13% from leading to trailing edge; assumption 2 seems reasonable.

Induced velocity w_p in Eq. (6) varies with AOA. To investigate the validity of assumption 3, Table 6 was produced. In a range of AOA 0–20 deg, the maximum increase of w_p is 25% over the entire testing domain. If AOA 0–10 deg is taken, then the maximum increase of w_p is 14.3%. Assumption 3 is reasonable when AOA is low but also when the throttle setting is large and the freestream velocity is low (Table 6). In horizontal flight, the AOA is always low. In near-hovering flight, the freestream velocity is small and the throttle setting is large, so assumption 3 is reasonable over the realistic flight domain, excepting transition.

The empirical factor k in Eq. (13) can be determined by imposing the condition that lift-curve slope increases slightly with increasing Reynolds number (over AOA 0–10 deg). The parameter k was varied

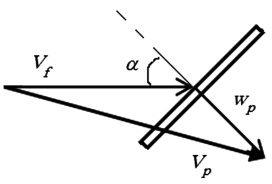

Fig. 21 Relationship between velocities.

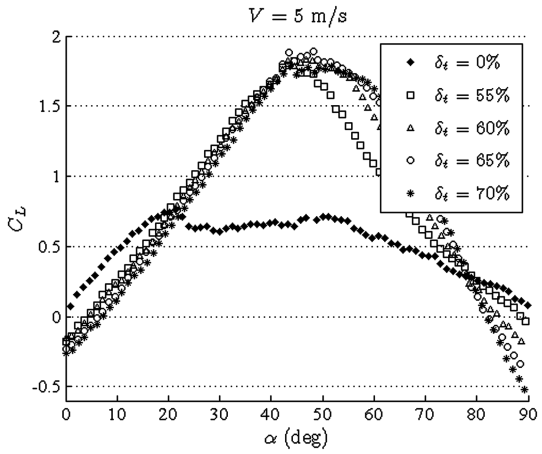

Fig. 22 Wing lift coefficient (proposed) $\delta_e = 0$ deg and $k = 0.19$.

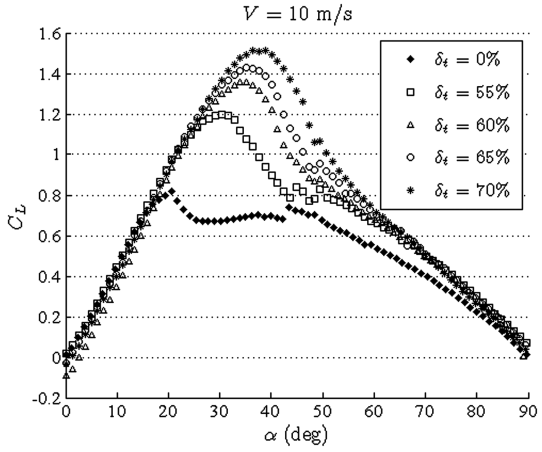

Fig. 23 Wing lift coefficient (proposed) $\delta_e = 0$ deg and $k = 0.19$.

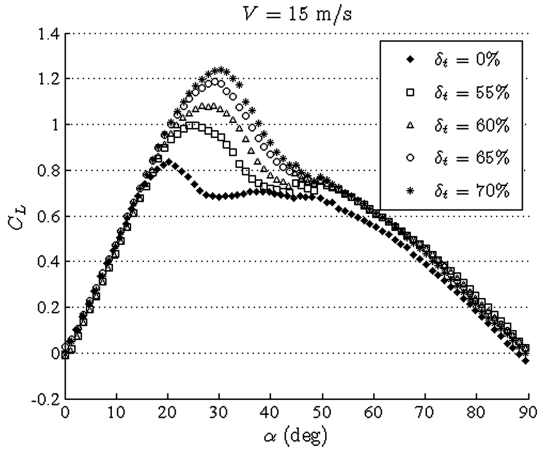

Fig. 24 Wing lift coefficient (proposed) $\delta_e = 0$ deg and $k = 0.19$.

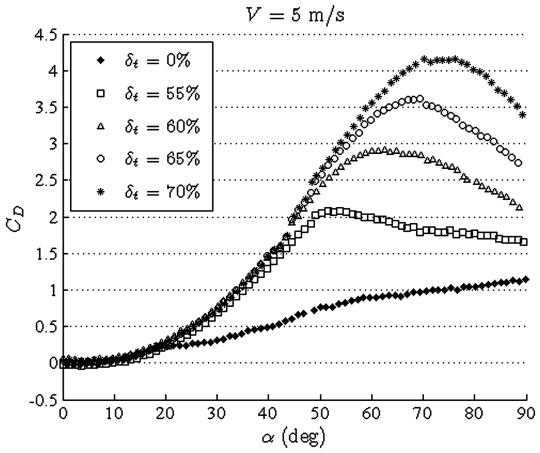

Fig. 25 Wing drag coefficient (proposed) $\delta_e = 0$ deg and $k = 0.19$.

in increments of 0.01, from 1 to 0, until the condition was met (best-fit curve slopes to C_L as a function of Re were employed to determine when the positive slope condition was achieved). The condition was first achieved for $k = 0.19$. Slopes and Reynolds numbers for empirically corrected coefficients are provided in Tables 7 and 8.

The relationship between the coefficient lift-curve slope and the Reynolds number is given by

$$dC_L/d\alpha \cong (3.19 \times 10^{-6}) \cdot Re + 2.347 \tag{16}$$

Lift coefficient plots were generated from the empirically corrected aerodynamic model with assumptions 1–4 assumed, and $k = 0.19$;

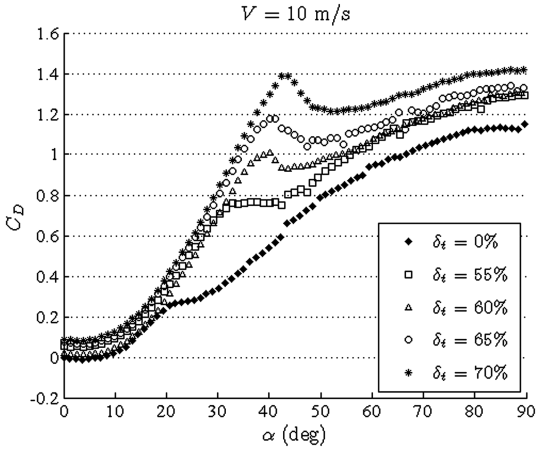

Fig. 26 Wing drag coefficient (proposed) $\delta_e = 0$ deg and $k = 0.19$.

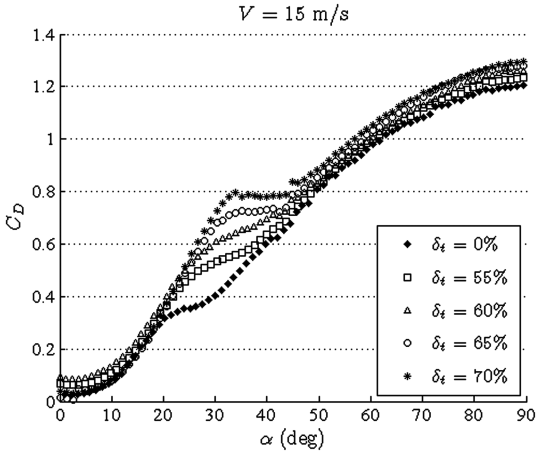

Fig. 27 Wing drag coefficient (proposed) $\delta_e = 0$ deg and $k = 0.19$.

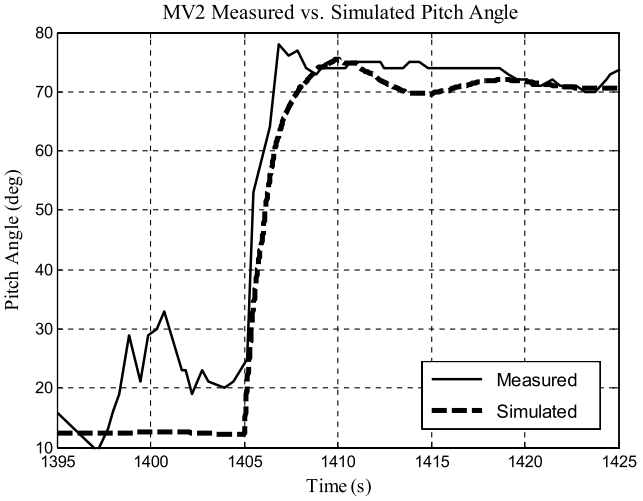

Fig. 28 Flight test vs data-based simulation [9] of MV2 pitch angle during transition maneuver.

they are given in Figs. 22–24. Drag coefficient results are shown in Figs. 25–27. It should be noted that better data collapse was obtained when assumptions 1–4 were not assumed, particularly in the stall region of the lift curves.

VIII. Conclusions

Typical MAV propulsion systems use brushless motors and an electronic speed controller. This study found that a contrarotating configuration exhibited very regular thrust behavior. Thrust varies quadratically with freestream velocity and linearly with throttle setting. The variation of thrust with AOA depends on the relative strength of the slipstream and the freestream. When the slipstream is relatively strong, the thrust-AOA curve is linear. When the slipstream is relatively weak, the thrust-AOA curve takes the form of a cubic polynomial with approximately zero slope at 0 and 90 deg AOA and an inflection point at approximately 45 deg AOA.

The effect of the slipstream on the wing is profound. At $V =$ 5 m/s, the slipstream delays stall by 24 deg and increases maximum wing lift by as much as 230%. Because the effect of the slipstream is strongly dependent on its strength relative to the freestream, a velocity ratio might be an appropriate defining parameter for further investigation. Elevator effectiveness increases with both freestream and slipstream strengths. For positive elevator deflections, stall AOA is reduced, the opposite is true for negative elevator deflections. At a moderate-to-high Reynolds number, maximum lift increases with positive elevator deflection and decreases with negative elevator deflection.

Drag curves are concave-up parabolic in their prestall region and concave-down parabolic in their poststall regions. As the slipstream strengthens, drag is increased throughout the entire AOA domain. In the stall region, maximum drag increases with positive elevator deflection and decreases with negative elevator deflection. At 90 deg AOA, drag is maximum at zero-elevator deflection. Wing aerodynamic efficiency is generally decreased by the slipstream.

Stall AOA increases with increasing slipstream-to-freestream velocity ratio. When the slipstream is present and freestream velocity approaches zero, the traditionally defined Reynolds number goes to zero and the traditionally defined lift and drag coefficients approach infinity.

An alternative definition of Reynolds number and aerodynamic coefficients based on a separate treatment of slipstream and freestream flows was proposed. Proposed coefficient lift-curve slope behavior was contrary to expectation with Reynolds number variation. Upon further consideration of the slipstream's effect on inertial and viscous forces, it was suspected that the slipstream disproportionately increases viscous force, due to its tendency to prematurely transition the wing's boundary layer to turbulence.

Estimation of model parameters was simplified. Predicted induced velocity was scaled down to compensate for its diminished Reynolds effect. The result was a straightforward empirical model that produces continuous, smooth, and finite coefficients over the entire domain.

Data from this study were used to determine parameters of a semiempirical model of wing aerodynamics, which was applied to a successful MAV dynamics simulator [9]. The simulator helps inform design tradeoffs, especially with regard to transition maneuvering (between horizontal and hovering flight). Simulator results compared favorably with MV2 flight test data, as seen in Fig. 28.

MV2 and the test model have several similarities. MV2 (Fig. 1b) has an S-shaped airfoil, and its wing is linearly tapered to approximate a Zimmerman planform. The test model incorporates a Zimmerman planform, and its airfoil is the same as that of MV2 but without thickness. The model uses the same contrarotating propulsion system as MV2, and it has the same elevon-to-wing area ratio.

MV2 exhibited a rapid response to pitch-up commands. The pitching rate of MV2 was estimated using onboard gyroscopes. The maximum pitching rate recorded during transition was 100 deg/s. Unsteady aerodynamic effects of rapid pitching will be investigated in a future study, which may include visualization of unsteady flowfields.

References

[1] Null, W., Noseck, A., and Shkarayev, S., "Effects of Propulsive-Induced Flow on the Aerodynamics of Micro Air Vehicles," 23rd AIAA Applied Aerodynamics Conference, AIAA Paper 2005-4626, Toronto, Canada, 2005.

[2] Shkarayev, S., Moschetta, J.-M., and Bataille, B., "Aerodynamic Design of Micro Air Vehicle for Vertical Flight," *Journal of Aircraft*, Vol. 45, No. 5, 2008, pp. 1715–1724. doi:10.2514/1.35573

[3] Kuhn, R. E., "Semiempirical Procedure for Estimating Lift and Drag Characteristics of Propeller-Wing-Flap Configurations for Vertical-and Short-Take-off-and-Landing Airplanes," NASA Memo 1-16-59L, Langley Field, VA, Feb. 1959.

[4] Kuhn, R. E., and Draper, J. W., "Investigation of the Aerodynamic Characteristics of a Model Wing-Propeller Combination and of the Wing and Propeller Separately at Angles of Attack up to 90°," NACA Rept. 1263, 1956.

[5] Hood, M. J., and Gaydos, M. E., "Effects of Propellers and Vibration on the Extent of Laminar Flow on the NACA 27-212 Airfoil," NACA ACR (WR L-784), 1939.

[6] Elsaadawy, E. A., and Britcher, C. P., "Effect of Propeller Slipstream on Heat-Exchanger Installations at Low Reynolds Number," *Journal of Aircraft*, Vol. 40, No. 4, 2003, pp. 751–758. doi:10.2514/2.3154

[7] Miley, S. J., Howard, R. M., and Holmes, B. J., "Wing Laminar Boundary Layer in the Presence of a Propeller Slipstream," *Journal of Aircraft*, Vol. 25, No. 7, 1988, pp. 606–611. doi:10.2514/3.45630

[8] Poinsot, D., Bérard, C., Krashanitsa, R., and Shkarayev, S., "Investigation of Flight Dynamics and Automatic Controls for Hovering Micro Air Vehicles," AIAA Guidance, Navigation and Control Conference, AIAA Paper 2008-6332, Aug. 2008.

[9] Chu, D., Sprinkle, J., Randall, R., and Shkarayev, S., "Simulator Development for Transition Flight Dynamics of a VTOL MAV," *International Journal of Micro Air Vehicles*, Vol. 2, No. 2, June 2010, pp. 69–89.

[10] "MP Jet Electromotor AC 22/4-60 D," MP Jet, Budejovice, Czech Republic, 2007.

[11] Uhlig, D. V., and Selig, M. S., "Post Stall Propeller Behavior at Low Reynolds Numbers," 46th AIAA Aerospace Sciences Meeting and Exhibit, AIAA Paper 2008-0407, Jan. 2008.

[12] Ol, M., and Zeune, C., "Analytical/Experimental Comparison for Small Electric Unmanned Air Vehicle Propellers," 26th AIAA Applied Aerodynamics Conference, AIAA Paper 2008-7345, Aug. 2008.

[13] McCormick, B. W., *Aerodynamics of V/STOL Flight*, Dover, New York, 1967.